

Lattice defect engineering advances n-type PbSe thermoelectrics

Received: 12 September 2024

Accepted: 7 January 2025

Published online: 14 January 2025

Qian Deng^{1,7}, Xiao-Lei Shi^{2,7}, Meng Li², Xiaobo Tan¹, Ruiheng Li¹, Chen Wang^{1,3}, Yue Chen^{1,3}, Hongliang Dong^{4,5}✉, Ran Ang^{1,6}✉ & Zhi-Gang Chen^{1,6}✉

Te-free thermoelectrics have garnered significant interest due to their immense thermoelectric potential and low cost. However, most Te-free thermoelectrics have relatively low performance because of the strong electrical and thermal transport conflicts and unsatisfactory compatibility of interfaces between device materials. Here, we develop lattice defect engineering through Cu doping to realize a record-high figure of merit of ~ 1.9 in n-type polycrystalline PbSe. Detailed micro/nanostructural characterizations and first-principles calculations demonstrate that Cu-induced interstitial defects and nanoprecipitates simultaneously optimize electron and phonon transport properties. Moreover, a robust Co/PbSe interface is designed to effectively prevent chemical reactions/diffusion; this interface exhibited a low electrical contact resistivity of $\sim 10.9 \mu\Omega \text{ cm}^2$, excellent durability, and good stability in the thermoelectric module, which achieves a record-high conversion efficiency of 13.1% at a temperature difference of 460 K in segmented thermoelectric modules. This study lays the groundwork for advancing the development of Te-free selenide-based thermoelectric materials.

Thermoelectric (TE) technology has significant potential for alleviating the global energy and environmental crisis, as it can directly convert waste heat into useful electrical energy in an environmentally friendly manner^{1–4}. However, the primary obstacles to the practical application of TE materials and devices are their low TE conversion efficiency and high cost^{5,6}. A high TE conversion efficiency requires reliable interface materials between TE materials and electrodes to prevent chemical reactions and diffusion, as well as high performance of the TE materials, which can be defined by the figure of merit $zT = S^2\sigma T/\kappa_{\text{tot}}$, where S , T , σ , and κ_{tot} are the Seebeck coefficient, absolute temperature in Kelvin, electrical conductivity, and total thermal conductivity [the sum of electronic (κ_{ele}) and lattice (κ_{lat}) parts], respectively. Over the past few decades, significant efforts have been made to increase the zT

value of materials, primarily by optimizing the carrier concentration (n_{H})^{7,8}, modulating the electronic structure^{1,9}, improving the power factor ($PF = S^2\sigma$), and designing unique crystal defects¹⁰ to increase phonon scattering to reduce κ_{lat} . However, most of these strategies for optimizing charge carrier and phonon transport have been aimed almost exclusively at independently enhancing electrical performance and reducing thermal transport¹¹, often with adverse effects on each other. Therefore, the bottleneck in improving the zT of materials lies in exploring a single, effective strategy that simultaneously optimizes both $S^2\sigma$ and κ_{lat} .

As a long-established TE material, PbTe has been used for power generation at intermediate temperatures (500–900 K) for a long time^{12–18}. However, due to the scarcity of Te in the Earth's crust (only

¹Key Laboratory of Radiation Physics and Technology, Ministry of Education, Institute of Nuclear Science and Technology, Sichuan University, Chengdu, China. ²School of Chemistry and Physics, ARC Research Hub in Zero-emission Power Generation for Carbon Neutrality, and Centre for Materials Science, Queensland University of Technology, Brisbane, QLD, Australia. ³Department of Mechanical Engineering, The University of Hong Kong, Hong Kong SAR, China. ⁴Center for High Pressure Science and Technology Advanced Research, Shanghai, China. ⁵Shanghai Key Laboratory of Material Frontiers Research in Extreme Environments (MFree), Institute for Shanghai Advanced Research in Physical Sciences (SHARPS), Shanghai, China. ⁶Institute of New Energy and Low-Carbon Technology, Sichuan University, Chengdu, China. ⁷These authors contributed equally: Qian Deng, Xiao-Lei Shi.

✉ e-mail: hongliang.dong@hpstar.ac.cn; rang@scu.edu.cn; zhigang.chen@qut.edu.au

0.001 ppm), the high material costs and insufficient sustainability have limited its widespread application. Due to the abundance of Se¹⁹, PbSe is a promising alternative to PbTe. PbSe has an electronic structure similar to that of PbTe^{1,20}, where the heavy Σ and light L valence bands have a small energy separation that degenerates with increasing temperature. This results in the zT value of p-type PbSe being significantly greater than that of n-type PbSe, which has only a single conduction band for transport. In fact, with continued research on p-type PbSe in recent years, its zT value at 900 K has approached -2.0 ^{21–23}. However, identifying practical strategies to improve n-type PbSe TE materials for matching is imperative for realizing high-performance TE devices (TEDs). To optimize the TE performance of n-type PbSe, although Cu doping has been shown to effectively optimize n_H over a wide temperature range^{8,24,25}, its doping mechanism has not been fully elucidated. Additionally, despite recent improvements in the performance of n-type PbSe polycrystals, the reliance on doping with multiple elements and high Te content, such as $\text{Pb}_{0.95}\text{Sb}_{0.033}\text{Se}_{0.6}\text{Te}_{0.4}$ ²⁶ and $\text{Pb}_{0.89}\text{Sb}_{0.012}\text{Sn}_{0.1}\text{Se}_{0.5}\text{Te}_{0.25}\text{S}_{0.25}$ ²⁷, complicates the preparation process and increases the cost.

In addition to optimizing the material performance, another challenge in current research on n-type PbSe is the design of compatible interface materials and further device integration. In TE modules, p-type and n-type materials (legs) are electrically connected in series

and thermally connected in parallel through metal electrodes (such as Cu, Ag, Ni, and their derivatives)^{5,28}. However, in practical applications, TE materials cannot be directly soldered to these electrode materials because they tend to diffuse into each other, reducing the TE performance, especially at high temperatures. For example, Ni and GeTe can form metal tellurides at interfaces, leading to decreased TE performance and cracking of the GeTe/Ni junction²⁸. Therefore, designing and identifying suitable TE interface materials (TEiMs) is crucial for developing efficient TE modules. Unfortunately, there are currently no systematic studies on the rational design and performance characterization of PbSe TEiMs. Consequently, there is an urgent need to develop high-performance n-type PbSe and compatible TEiMs to construct efficient and reliable PbSe-based TEDs.

Here, we propose a rational design strategy based on Cu-doped lattice defect engineering to fill the above research gap. This involves utilizing a high level of Cu doping to achieve interstitial Cu (Cu_i) defects while simultaneously inducing the formation of a large number of uniformly distributed nanoscale semicoherent precipitates. This approach effectively regulates n_H and transport properties, significantly enhancing S and $S^2\sigma$ (Fig. 1a). Moreover, the κ_{lat} is reduced by synergistically enhancing the scattering of phonons with different wavelengths, ultimately achieving ultrahigh TE performance for n-type PbSe, which is highly competitive with reported values (Fig. 1b)^{7,9,27,29–31}.

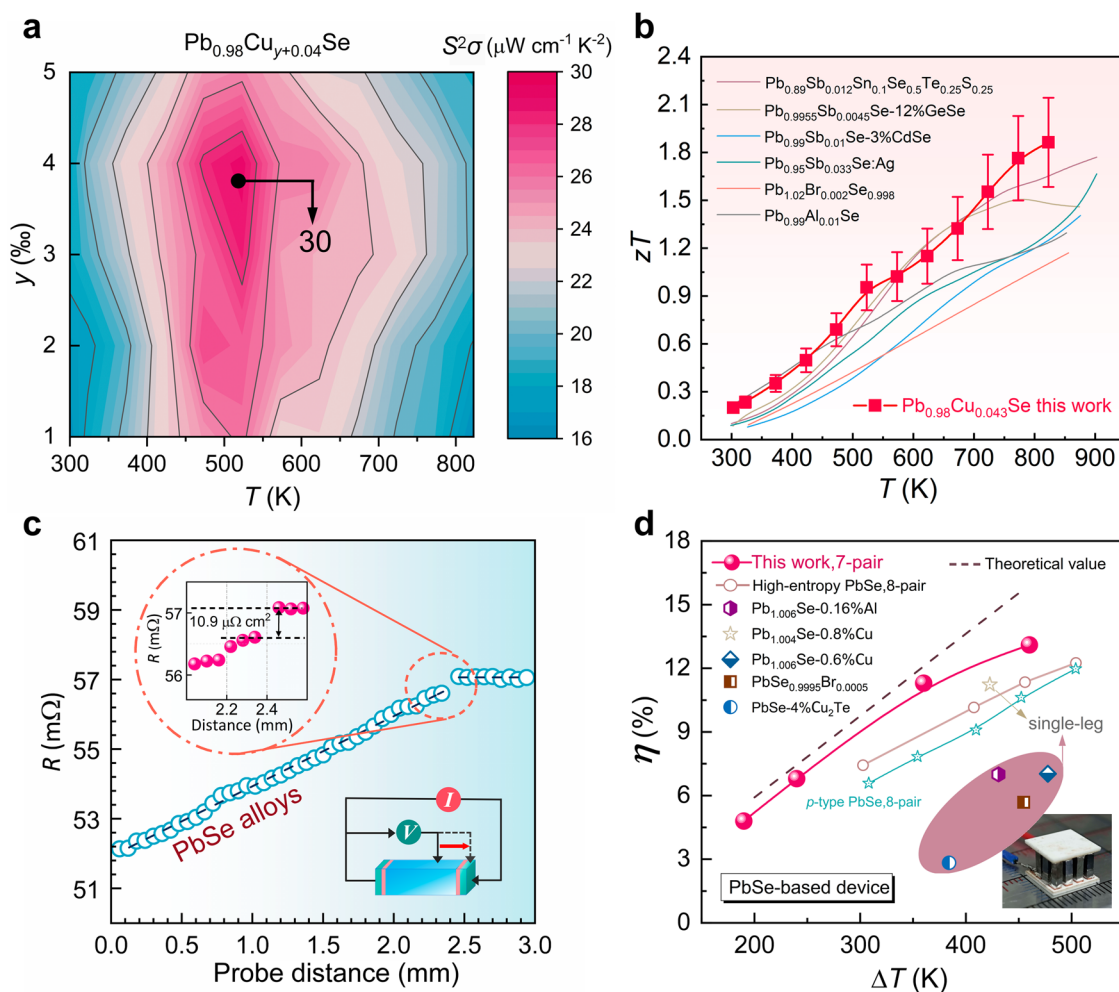


Fig. 1 | Introduction of advancing n-type PbSe-based thermoelectrics through the elaborate manipulation of compositions and screening of stable thermoelectric interface materials (TEiMs). a Power factor ($S^2\sigma$) as a function of y and temperature (T) for $\text{Pb}_{0.98}\text{Cu}_{y+0.04}\text{Se}$. **b** T -dependent figure of merit (zT) for n-type $\text{Pb}_{0.98}\text{Cu}_{0.043}\text{Se}$ in comparison with other state-of-the-art n-type PbSe^{7,9,27,29–31}. Error

bars of 15% are applied. **c** Room-temperature electrical contact resistivity (ρ_c) for the Co/PbSe junction based on the four-probe technique (inset in c). **d** Conversion efficiencies (η) for our $\text{Pb}_{0.98}\text{Cu}_{0.043}\text{Se}$ -based segmented module and the literature results^{23,27,32–36}. The inset shows a photo of our $\text{Pb}_{0.98}\text{Cu}_{0.043}\text{Se}$ -based segmented module.

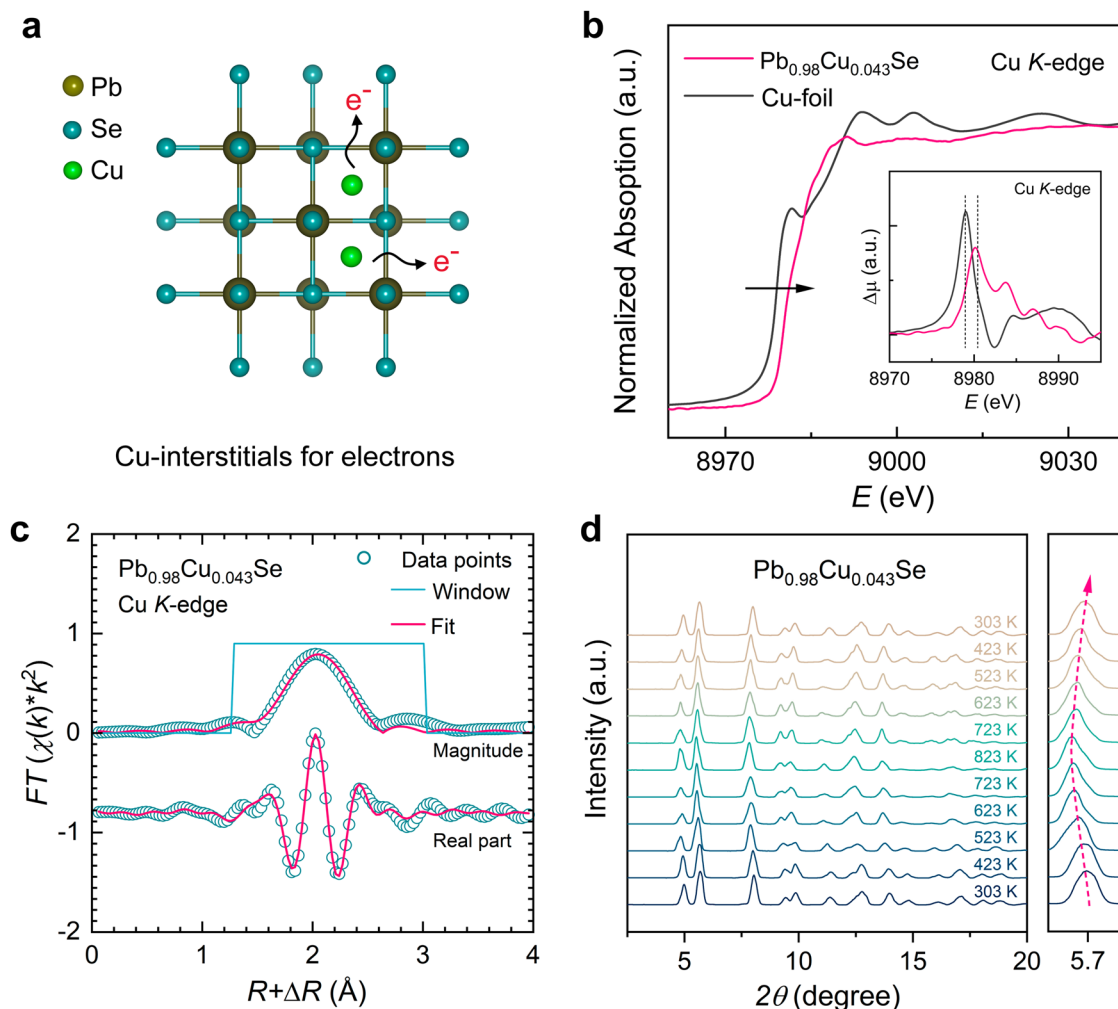


Fig. 2 | Crystal structures obtained via synchrotron radiation measurements. **a** Schematic diagram of the interstitial Cu (Cu_i) in the PbSe lattice. **b** The Cu K-edge X-ray absorption near-edge structure (XANES) spectra of the Pb_{0.98}Cu_{0.043}Se (y = 0.003) sample and a Cu foil. The insets in **(b)** are the corresponding difference

curves. **c** Radial distributions surrounding Cu and their corresponding real-part components (solid lines and open circles are the fitted and experimental values) for Pb_{0.98}Cu_{0.043}Se. **d** Variable-temperature synchrotron radiation X-ray diffraction (SXRD) pattern of Pb_{0.98}Cu_{0.043}Se (first measurement).

In addition, regarding the design of device interfaces, we conducted a detailed characterization of ten candidate TEIMs and demonstrated that Co can serve as a reliable diffusion barrier for high-performance PbSe. The Ag/Co/PbSe interface design successfully prevented chemical reactions and diffusion, with negligible additional resistance (Fig. 1c). This contributed to a high conversion efficiency (η) of ~13.1% under a temperature difference (ΔT) of 460 K in segmented TED (Fig. 1d), which is significantly superior to the η of previously reported PbSe-based TEDs^{23,27,32–36}.

Results and discussion

Design principle and structure characterization of the materials

We first calculated the defect formation energies (E_{def}) of potential Cu-related defects in the PbSe system based on density functional theory. These defects include Cu_i, substitution-interstitial Cu pairs (Pb₃₁Cu₂Se₃₂), and Cu/Pb substitution (Cu_{Pb}) to understand the possible doping mechanisms of Cu^{37–40}. The calculation results indicate that Pb₃₁Cu₂Se₃₂ has the lowest E_{def} (Supplementary Fig. 1 and Supplementary Table 1), suggesting that intentionally introducing cation vacancies in PbSe can promote the formation of more Cu_i to some extent, thereby increasing n_{H} . Therefore, to obtain low-cost, high-performance n-type PbSe TE materials, we designed the Pb_{1-x}Cu_{2x+y}Se system [Pb_{1-x}Cu_{2x+y}Se → xCu₂Se + yCu_i + (1-x)PbSe] based on the E_{def}

results and the following four aspects. First, the Cu⁺ ions occupying the interstitial site (Cu_i) in PbSe are ideal electron donors⁵ for ensuring n-type conductivity (Fig. 2a). Second, considering the low solubility of Cu in PbSe⁸, the addition of excess Cu induces complex crystal defects, such as the highly anharmonic liquid-like Cu₂Se⁴¹ and other solute-rich defects⁸, which significantly suppress κ_{lat} . Third, we aim to reveal the microstructural evolution of the dopant content and the potential crystallographic relationship between the nanostructures and the PbSe matrix and explore how these factors affect the TE properties. Finally, controlling Cu doping simplifies the material preparation process and reduces costs.

The powder X-ray diffraction (XRD) patterns of Pb_{1-x}Cu_{2x+y}Se indicate that the prepared samples can be entirely classified as having a NaCl structure. With increasing x and y values, the lattice parameter remains nearly unchanged but expands slightly in Pb_{1-x}Cu_{2x+0.002}Se ($x = 0, 0.01, 0.02, 0.03, \text{ and } 0.04$) (Supplementary Fig. 2) and Pb_{0.98}Cu_{0.04+y}Se ($y = 0.001, 0.002, 0.003, 0.004, \text{ and } 0.005$) (Supplementary Fig. 3). The former is primarily attributed to the formation of semicoherent Cu₂Se nanostructures, while the latter involves more Cu entering the interstitial lattice of PbSe. To determine the local structure of the Cu-doped samples, we performed X-ray absorption fine structure (XAFS) spectroscopy to identify the local coordination environment for the absorbing atomic center⁴². Figure 2b shows the

normalized X-ray absorption near-edge structure (XANES) spectra of the Cu *K*-edge. For the $\text{Pb}_{0.98}\text{Cu}_{0.043}\text{Se}$ ($y = 0.003$) sample, the position of the Cu absorption edge shifts noticeably to a higher energy than that of Cu foil, indicating an increase in the oxidation state of Cu. We fitted the least squares extended XAFS (EXAFS) curves for the first coordination shell of Cu using the Cu–Se backscattering pathway⁴³. The results show a high degree of consistency between the experimental data and theoretical curves, indicating that most of the Cu atoms form a Cu_2Se phase (Fig. 2c and Supplementary Table 2). The Se *K*-edge XANES spectra of the representative samples are presented in Supplementary Fig. 4. It is evident that the Se absorption edge for all samples shifts towards the high-energy side relative to the Se foil (Supplementary Fig. 4b). Notably, the Se *K*-edge absorption energy in the Cu-doped samples is in line with that of the pristine PbSe, revealing that Se retains a valence state of -2 . Based on these results, Cu is in the $+1$ valence state in the Cu-doped samples. Compared with that of pristine PbSe, the distance between Se and the first-shell atom was shorter in the $\text{PbCu}_{0.002}\text{Se}$ ($x = 0$) and $\text{Pb}_{0.98}\text{Cu}_{0.042}\text{Se}$ ($x = 0.02$) samples (Supplementary Fig. 5 and Supplementary Table 3). This decrease is attributed to the formation of Cu_i and Cu_2Se precipitates, which bring the Cu atoms in the first coordination shell of Se closer to Pb, thereby shortening the Se–Pb distance. The Debye–Waller factor (B) increases from 0.017 to 0.021 \AA^2 with increasing x content (Supplementary Table 3). This matches the refinement results of XRD (Supplementary Fig. 6), indicating enhanced atomic disorder. Additionally, we performed high-precision synchrotron radiation X-ray diffraction (SXRD) measurements on the $\text{Pb}_{0.98}\text{Cu}_{0.043}\text{Se}$ ($y = 0.003$) sample over a temperature range from 303 to 823 K. No additional characteristic diffraction peaks were observed across the temperature range, and the main peak shifted to a lower angle than expected due to temperature-induced lattice expansion (Fig. 2d). Furthermore, the results of the repeatability tests have substantiated its excellent stability (Supplementary Fig. 7).

Atomic-scale evolution of nanodefects with increasing Cu dopant content

To directly observe the microstructural evolution in the PbSe matrix caused by different Cu doping levels, we conducted atomic-resolution scanning transmission electron microscopy (STEM) characterization. For the $\text{PbCu}_{0.002}\text{Se}$ ($x = 0$) sample, the introduction of trace amounts of Cu created a dense dislocation network within the matrix (Supplementary Fig. 8a–d). It has been demonstrated that introducing dislocations in lead chalcogenides can effectively scatter mid-wavelength phonons and reduce κ_{lat} ^{18,24}. With a slight increase in the Cu doping content, several nanoscale Cu_i nanoclusters are exposed within the matrix^{8,44,45}, which is consistent with the low E_{def} of Cu_i in PbSe. These nanoclusters are metastable regions within PbSe that form Guinier–Preston (GP) zones⁴⁶ and serve as nucleation precursors for the formation of larger and more stable Cu_2Se precipitates. Thus, with a further increase in the Cu doping content, a large number of uniformly distributed Cu-rich precipitates are embedded within the matrix (Supplementary Fig. 9). Considering that the sample synthesis was carried out under prolonged annealing (for five days), we suppose that the large Cu_2Se precipitates grow by consuming the metastable Cu_i nanoclusters through the Ostwald ripening mechanism⁴⁷.

The low-magnification high-angle annular dark-field (HAADF) and annular bright-field STEM images of the $\text{Pb}_{0.98}\text{Cu}_{0.042}\text{Se}$ ($x = 0.02$) sample show denser dislocation clusters (Supplementary Fig. 8e, f) and abundant nanoscale Cu_2Se plate-like precipitates (Fig. 3a and Supplementary Fig. 8e–h), respectively. Despite its simple chemical formula, Cu_2Se has a rather complex atomic arrangement, especially in the room-temperature α -phase^{48–51}. Specifically, within the lattice, Se anions and Cu cations form a rigid cubic sublattice and a liquid-like sublattice (Fig. 3b, c), respectively. Moreover, accurately observing the connection structure between complex

precipitates and the TE matrix at the atomic scale has been a significant challenge. This has led to almost all precipitated phases being merely phonon scattering sources, while their impact on carrier transport has been overlooked. Therefore, determining the orientation relationship (OR) between Cu_2Se nanoprecipitates and the PbSe matrix is crucial for understanding the mechanism behind abnormal TE enhancement. Figure 3d and e clearly show atomic-resolution HAADF-STEM images of the sharp interfaces of the $\text{Cu}_2\text{Se}/\text{PbSe}$ nanocomposites along different zone axes. Based on the crystallographic analysis, the ORs are $[101]_{\text{PbSe}} \parallel [10\bar{1}]_{\text{Cu}_2\text{Se}}$ and $[110]_{\text{PbSe}} \parallel [0\bar{1}0]_{\text{Cu}_2\text{Se}}$ (Supplementary Figs. 10 and 11). Due to the slight lattice mismatch between these parallel planes (less than 5%, Supplementary Table 4), semicoherent interfaces are constructed between the Cu_2Se nanoprecipitates and the PbSe matrix, which supports the nearly constant lattice parameters of the $\text{Pb}_{1-x}\text{Cu}_{2x+0.002}\text{Se}$ samples with increasing x content (Supplementary Fig. 2). The representative extra half-atomic plane in the $\text{Pb}_{0.98}\text{Cu}_{0.042}\text{Se}$ ($x = 0.02$) matrix is marked by a Burger vector (red arrow) of $1/2[101]$ (Fig. 3f). The corresponding geometric phase analysis (GPA) reveals a significant linear strain field near the dislocation core (inset in Fig. 3f), which enhances phonon scattering. Figure 3g shows an atomic schematic diagram corresponding to Fig. 3d. The unique semicoherent phase enhances the electrical transport properties while further scattering phonons. Interestingly, compared with that in the $\text{Pb}_{0.98}\text{Cu}_{0.042}\text{Se}$ ($x = 0.02$) sample, the number of precipitates in the $\text{Pb}_{0.96}\text{Cu}_{0.082}\text{Se}$ ($x = 0.04$) sample increases, as expected. However, the number of dislocations unexpectedly decreased, and the dislocations were pinned around the semicoherent Cu_2Se nanoprecipitates (Supplementary Fig. 8i), leading to anomalous changes in both n_{H} and κ_{lat} .

Ultrahigh thermoelectric performance

The temperature-dependent carrier transport characteristics are significantly influenced by the Cu doping content. The results from Hall measurements for $\text{Pb}_{1-x}\text{Cu}_{2x+0.002}\text{Se}$ are shown in Fig. 4a, b. For the sample with $x = 0$, the n_{H} remains nearly constant below 520 K but increases sharply with increasing temperature, attributed to the dynamic doping effect⁸. For samples with $x = 0.01$ – 0.04 , the n_{H} increases significantly. This trend supports the calculated E_{def} of Cu, suggesting that introducing Pb vacancies facilitates the generation of more Cu_i . Furthermore, the unusual decrease in n_{H} of $\text{Pb}_{1-x}\text{Cu}_{2x+0.002}\text{Se}$ ($x = 0.01$ – 0.04) between 400 and 520 K is attributed to the transformation of α -phase Cu_2Se into cubic β -phase Cu_2Se ^{45,48}, as confirmed by differential scanning calorimetry (Supplementary Fig. 12). The substantial increase in the hole concentration in the Cu_2Se material, triggered by the phase transition near 400 K, further confirms the corresponding decrease in the electron concentration^{6,48–50}. The dynamic Cu doping behavior of PbSe is attributed to the high mobility of Cu ions within the rigid cubic lattice formed by Se anions in Cu_2Se precipitates, which move to interstitial positions in PbSe⁴⁵. This behavior is further validated by the semicoherent interface observed between the Cu_2Se precipitates and the PbSe matrix. The tightly connected interface minimizes the lattice mismatch at the phase boundary, creating a favorable pathway for the rapid migration of Cu ions into the lattice gaps of PbSe at high temperatures, as indicated by the red arrow in Fig. 3g. The rapid movement of Cu ions in Cu_2Se also occurs above 500 K^{41,52}, aligning with the temperature at which self-optimization of n_{H} is observed (Fig. 4a). Specifically, the dynamic behavior of Cu originates from the phenomenon that temperature drives the Cu ions of the semicoherent Cu_2Se precipitates in the matrix to enter the lattice gap of PbSe.

Figure 4b shows the temperature-dependent carrier mobility (μ_{H}) of the $\text{Pb}_{1-x}\text{Cu}_{2x+0.002}\text{Se}$ ($x = 0$ – 0.04) samples. The μ_{H} of $\text{PbCu}_{0.002}\text{Se}$ ($x = 0$) sample exhibits a consistent trend ($\mu_{\text{H}} \sim T^{-2.5}$) with that reported for the PbCu_iSe system in the literature⁸, confirming that the dominant carrier scattering mechanism in these samples is primarily governed

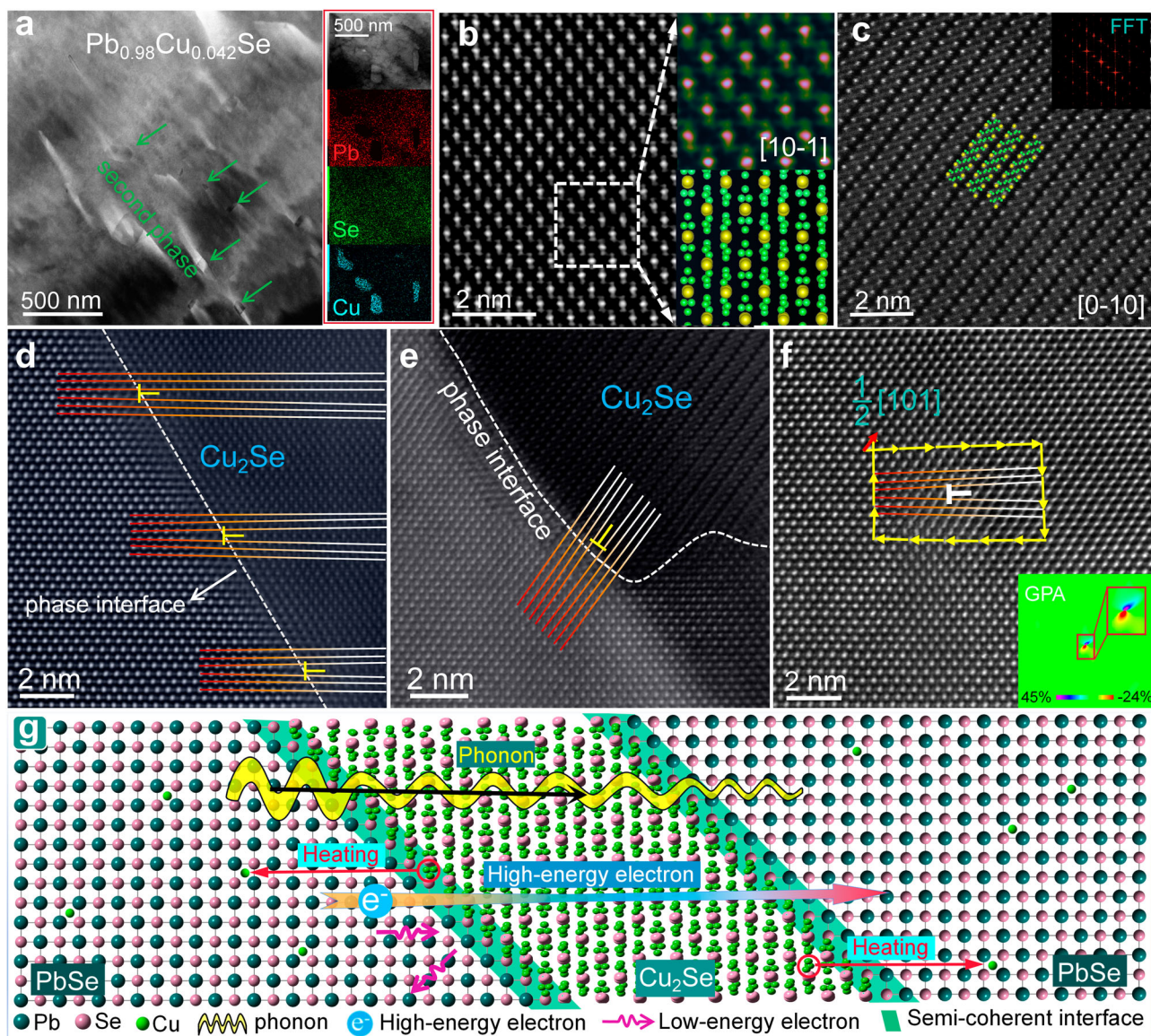


Fig. 3 | Atomic micro/nanostructural characterization of $\text{Pb}_{0.98}\text{Cu}_{0.042}\text{Se}$ ($x = 0.02$). **a** Low-magnification scanning transmission electron microscopy (STEM) image displaying dense Cu-rich nanoprecipitates (denoted by the green arrows). **b, c** Atomic-resolution STEM images and corresponding atomic model clearly indicating the structure of Cu_2Se along the [10-1] and [0-10] zone axes, respectively. The inset in (c) is the corresponding fast Fourier transform (FFT) image. **d, e** High-resolution high-angle annular dark-field (HADF) STEM images of the semi-coherent interfaces at the phase boundary between the Cu_2Se nanoprecipitate and

PbSe matrix viewed along different zone axes. The phase interfaces and dislocations are marked by dashed lines and yellow symbols respectively. **f** High-resolution HADF-STEM image of a typical dislocation. The yellow arrows give a complete Burgers loop of a dislocation, and the estimated Burgers vector (red arrow) is $\mathbf{B}_D = 1/2[101]$. The dislocation is marked by white symbols. The inset image shows the geometric phase analysis (GPA) strain analysis of the entire area in (f). **g** Illustration of the semicoherent Cu_2Se nanoprecipitates and influence on phonon and electron transport.

by acoustic phonons^{7,8,25,53,54}. However, for samples with $x > 0$, the μ_H significantly deviates from the $T^{-2.5}$ behavior. Both σ and S are displayed in Supplementary Fig. 13. The theoretical Pisarenko relationship⁵⁵ is simulated based on acoustic phonon-dominated charge transport. The absolute S ($|S|$) data for $\text{PbCu}_{0.002}\text{Se}$ ($x = 0$), along with the reported values for $\text{PbCu}_{0.005}\text{Se}$ ⁸ and Br-doped PbSe ⁷, align well with the same theoretical curves (Fig. 4c). This consistency confirms that the addition of Cu_i does not alter the conduction band structure of PbSe ^{8,24,25}. The same carrier effective mass (m^*) of the $x = 0$ sample and Br-doped PbSe ⁷ at various temperatures (Supplementary Fig. 14) also provides strong support for this conclusion. Unexpectedly, the experimental $|S|$ values for samples with $x = 0.01$ – 0.04 are significantly higher than the theoretical values. We calculated the effect of substitution-intrinsic Cu pairs on the density of states effective mass^{37–39} of n-type PbSe based

on the minimum E_{def} of Cu (for more details, see the Supplementary Information). There was no significant change in m^* near the Fermi level (Supplementary Fig. 15), indicating that the increase in $|S|$ was attributed to the energy filtering effect rather than alterations in the electronic structure⁵⁶. This conclusion is further supported by the anomalous variations observed in the temperature-dependent μ_H (Fig. 4b). The energy filtering effect arises from the band bending caused by the dense Cu_2Se nanoprecipitates, which create a slowly varying potential that hinders the movement of low-energy carriers⁵⁷ (Figs. 3g and 4d). Since the carrier scattering for the sample with $x = 0$ is dominated by acoustic phonons, the scattering factor r_0 should be -0.5 at room temperature. The ratio of the scattering parameter $r_x + 1$ for $\text{Pb}_{1-x}\text{Cu}_{2x+0.002}\text{Se}$ ($x = 0.01$ – 0.04) to $r_0 + 1$ for $x = 0$ can be calculated⁵⁸ using the formula $S = [8\pi^2 k_B^2 / (3h^2 e)] m^* T [\pi / (3n)]^{3/2} (r_x + 1)$,

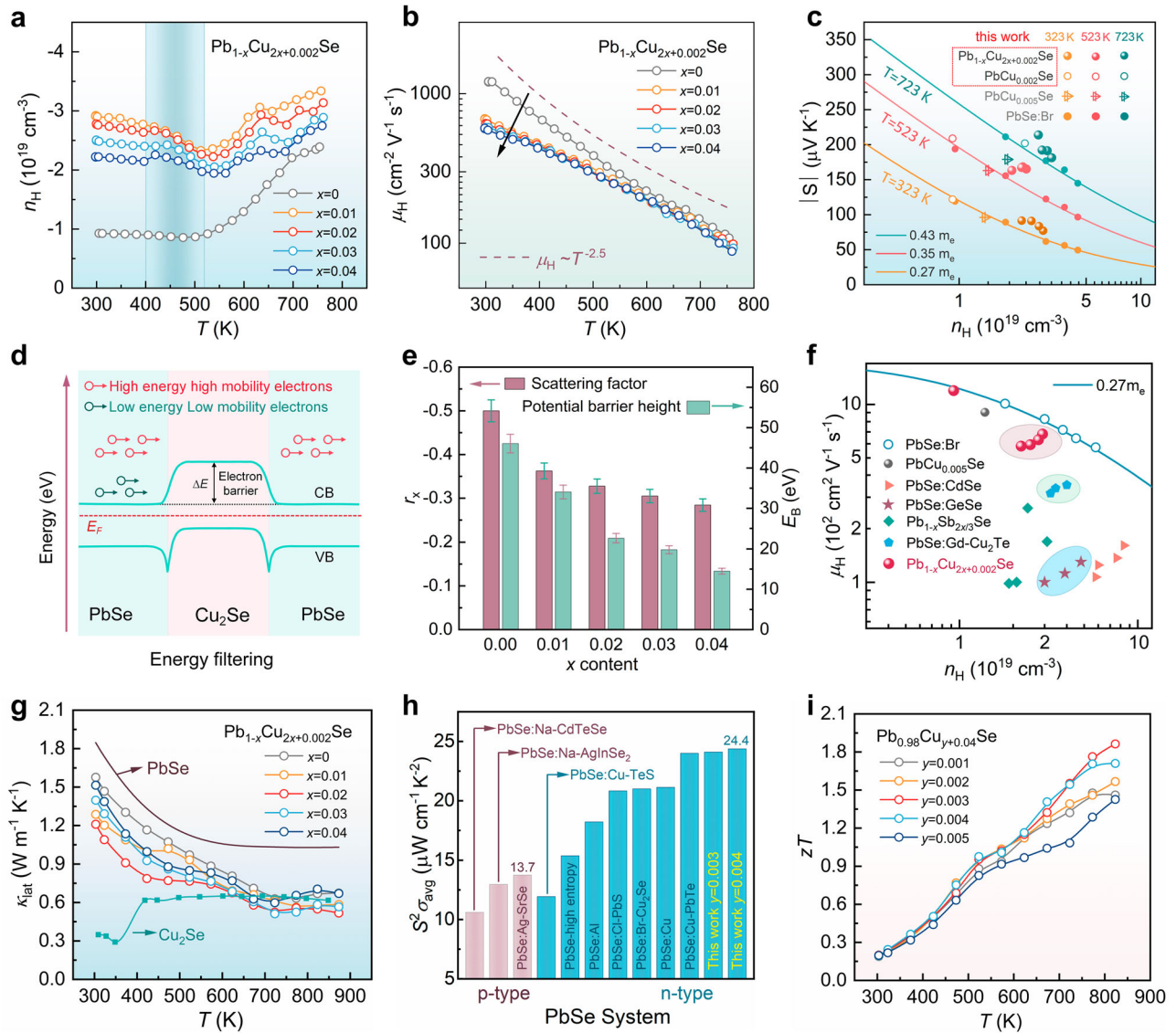


Fig. 4 | Thermoelectric properties of $\text{Pb}_{1-x}\text{Cu}_{2x+0.002}\text{Se}$ and $\text{Pb}_{0.98}\text{Cu}_{y+0.04}\text{Se}$. Temperature-dependent **a** carrier concentration (n_H) and **b** mobility (μ_H) for $\text{Pb}_{1-x}\text{Cu}_{2x+0.002}\text{Se}$. The black arrow serves as a guide to show the trend of μ_H . **c** The variation in the n_H of the absolute S ($|S|$) at different temperatures. m_e is the free electron mass. The reported experimental data for n-type $\text{PbCu}_{0.005}\text{Se}$ ⁸ and Br-doped PbSe ⁷ are represented by solid circles. **d** Schematic diagram of the energy barrier between the Cu_2Se precipitates and the PbSe matrix. The potential barrier at the conduction band (CB) can selectively block low-energy electrons. E_F and VB are

the Fermi energy and the valence band, respectively. **e** Calculated scattering parameter (r_x) and interface potential barrier (E_B) for $\text{Pb}_{1-x}\text{Cu}_{2x+0.002}\text{Se}$. Error bars of 5% are applied. **f** n_H as a function of μ_H for $\text{Pb}_{1-x}\text{Cu}_{2x+0.002}\text{Se}$, along with literature data for representative n-type PbSe systems^{7,9,29,30,35}. **g** Temperature-dependent lattice thermal conductivity (κ_{lat}) of PbSe , $\text{Pb}_{1-x}\text{Cu}_{2x+0.002}\text{Se}$ and the reported Cu_2Se ⁴⁸. **h** Average $S^2\sigma$ ($S^2\sigma_{\text{avg}}$) from 303 to 823 K for $y = 0.003$ and 0.004 samples, compared with reported high-performance PbSe ^{8,21,23-25,27,31,62-64}. **i** Temperature-dependent figure-of-merit (zT) for $\text{Pb}_{0.98}\text{Cu}_{y+0.04}\text{Se}$.

where k_B , h , and e represent the Boltzmann constant, Planck constant, and electron charge, respectively. Thus, the ratio $(r_x + 1)/(r_0 + 1)$ can be written as⁵⁸:

$$\frac{r_x + 1}{r_0 + 1} = \frac{S_x}{S_0} \left(\frac{n_x}{n_0} \right)^{2/3} \quad (1)$$

As shown in Fig. 4e, the scattering factor r_x exhibits a positive correlation, confirming that the increase in S is due to the increase in r_x caused by the formation of sufficient nanoprecipitates. The linear fitting of $\ln(\sigma T^{1/2})$ and $1/(k_B T)$ for the $\text{Pb}_{1-x}\text{Cu}_{2x+0.002}\text{Se}$ ($x = 0-0.04$) samples (Supplementary Fig. 16) can effectively evaluate the interface potential barrier (E_B)⁵⁹. The E_B in the matrix decreases with increasing x content (Fig. 4e), validating that the semicoherent Cu_2Se material benefits carrier transport, which is consistent with the nearly equal μ_H

for $x = 0.01-0.04$ samples (Supplementary Fig. 17a). The room-temperature μ_H of $\text{PbCu}_{0.002}\text{Se}$ sample in this work is higher than that of $\text{PbCu}_{0.005}\text{Se}$ sample reported in the literature⁸, as the carrier and defect scattering in our sample is less pronounced, as illustrated in Fig. 4f. In particular, compared to other reported n-type PbSe systems^{7,9,29,30,35}, the $\text{Pb}_{1-x}\text{Cu}_{2x+0.002}\text{Se}$ samples exhibit distinct μ_H values for the same n_H (Fig. 4f), further highlighting the advantage of the semicoherent interface. By introducing dense and uniformly distributed Cu_2Se nanoprecipitates into the matrix, we achieved the combined effect of self-optimization of n_H in the mid-temperature range and compensation for the intrinsically low $|S|$ of PbSe . This significantly enhances the $S^2\sigma$ of $\text{Pb}_{1-x}\text{Cu}_{2x+0.002}\text{Se}$ ($x = 0.01-0.04$) across temperatures from 500 to 873 K (Supplementary Fig. 17b).

The thermal transport properties of $\text{Pb}_{1-x}\text{Cu}_{2x+0.002}\text{Se}$ are shown in Supplementary Fig. 18 and Fig. 4g. Compared with that of pristine

PbSe, κ_{lat} is significantly suppressed for $\text{Pb}_{1-x}\text{Cu}_{2x+0.002}\text{Se}$ (Fig. 4g). When $x \leq 0.02$, the reduction in κ_{lat} is due to the stronger phonon scattering caused by the increase in dislocation and nanoprecipitate density. Although the number of nanoprecipitates continues to rise with higher doping levels ($x > 0.02$), the dislocations with a size similar to the phonon mean free path⁶⁰ is greatly reduced, which leads to a slight increase of κ_{lat} . Supplementary Fig. 19a indicates that the κ_{lat} of conventional element-doped PbSe, such as Cd⁹, Te²⁶, Cr⁶¹, and Ga⁶², decreases along the power law of $-T^{-1}$. In contrast, the κ_{lat} of high-content Cu-doped PbSe exhibits a complex trend with increasing temperature^{8,25,44,63}, as shown in Fig. 4g and Supplementary Fig. 19b. Research usually focuses only on reducing κ_{lat} ^{8,25,44,63} and discussing its origin in the PbSe system while neglecting the abnormal changes in κ_{lat} near 400 K. The experimental κ_{lat} of CuSe⁴⁸ is shown in Fig. 4g. Obviously, the κ_{lat} in Cu₂Se suddenly increases from 0.25 to 0.58 W m⁻¹ K⁻¹ at ~400 K (other TE parameters in Supplementary Fig. 20). Hence, the κ_{lat} for $\text{Pb}_{1-x}\text{Cu}_{2x+0.002}\text{Se}$ ($x = 0.01-0.04$) slowly decreases and even plateaus from 400 to 550 K, which is the signal of the Cu₂Se phase transition. In brief, when a large number of semi-coherent Cu₂Se nanoprecipitates enter the PbSe matrix, the electrical performance is distinctly enhanced, and the thermal transport is synergistically optimized, leading to an improvement in the TE performance of n-type PbSe (Supplementary Fig. 21).

Considering that the sample with $x = 0.02$ in $\text{Pb}_{1-x}\text{Cu}_{2x+0.002}\text{Se}$ ($x = 0-0.04$) has the lowest κ_{lat} and the highest zT of 1.63, the $\text{Pb}_{0.98}\text{Cu}_{y+0.04}\text{Se}$ ($y = 0.001-0.005$) samples were further optimized to advance PbSe TE materials. As expected, the room-temperature n_{H} increases with increasing y content (Supplementary Fig. 22a) since additional Cu occupies the interstitial position of the PbSe lattice to provide electrons. The electrical parameters (n_{H} , μ_{H} , σ , S) are shown in Supplementary Fig. 22b–e. The addition of excess Cu does not distinctly alter the carrier scattering mechanism (Supplementary Fig. 22c), resulting in $|S|$ still maintaining an enhancement superiority at the same n_{H} (Supplementary Fig. 22f). Therefore, an outstanding $S^2\sigma$ is achieved by further optimizing n_{H} compared with that of the $\text{Pb}_{0.98}\text{Cu}_{0.042}\text{Se}$ ($x = 0.02$) sample (Fig. 1a). Notably, the ultrahigh average $S^2\sigma$ ($S^2\sigma_{\text{avg}}$) for the $y = 0.004$ sample, measured from 303 to 823 K, reaches $-24.4 \mu\text{W cm}^{-1}\text{K}^{-2}$, surpassing most reported values for high-performance PbSe systems^{8,21,23-25,27,31,63-65} (Fig. 4h). The thermal parameters (κ_{tot} , κ_{ele} , κ_{lat}) for $\text{Pb}_{0.98}\text{Cu}_{y+0.04}\text{Se}$ ($y = 0.001-0.005$) are shown in Supplementary Fig. 23a–c. The κ_{lat} is significantly suppressed with increasing y content, reaching an ultralow value of $-0.25 \text{ W m}^{-1}\text{K}^{-1}$ (Supplementary Fig. 23c), which is close to the theoretical limit of $-0.23 \text{ W m}^{-1}\text{K}^{-1}$ ⁶⁶. Eventually, the peak zT value reaches -1.9 (Fig. 4i and Supplementary Fig. 24d). This is almost the highest value among all the n-type PbSe-based TE materials and is comparable to that of n-type PbTe^{14} (Supplementary Fig. 23d).

Screening of TEiMs and manufacturing of high-performance modules

High-performance materials must fully utilize their potential at the device level, which largely depends on matching TEiMs, particularly at high temperatures. In this work, we employed a high-throughput screening strategy⁶⁷ to expedite the identification of potential TEiMs for PbSe. Powders of ten candidate metals (Ti, Zr, V, Cr, Mn, Ni, Nb, Mo, Fe, and Co) were mixed with undoped PbSe powder and sintered according to the standard parameters for PbSe TE materials. Energy dispersive spectroscopy (EDS) scanning analysis and scanning electron microscopy (SEM) images of the representative interface microstructures between these metals and PbSe are shown in Supplementary Figs. 25–29. These metals can be categorized into three groups based on their reaction with PbSe. The first group includes Ti, Zr, V, and Cr, which exhibit minimal reactions with Se and form corresponding compounds, consistent with their binary phase diagrams (Supplementary Figs. 25 and 26). The second group consists of Mn, Ni,

Nb, and Mo. Among them, Mn and Ni undergo significant selenization, likely due to their relatively low melting points (Supplementary Fig. 27). On the other hand, Nb and Mo form well-alloyed phases with Pb and PbSe, respectively (Supplementary Fig. 28). Due to the short duration of the sintering process, the metals in the first and second groups are unsuitable as TEiMs for PbSe. The third group included Fe and Co, which exhibited excellent chemical inertness after sintering and formed strong bonds with the PbSe matrix (Supplementary Fig. 29).

In addition to chemical inertness, a compatible TEiM must also form a low-energy-loss interface with TE materials, ensuring a lower electrical contact resistance (ρ_c) at the junction. To evaluate this phenomenon, we used a one-step hot pressing method to fabricate PbSe single legs with Co and Fe as TEiMs. The ρ_c of the Co/PbSe junction is $-10.9 \mu\Omega \text{ cm}^2$ (Fig. 1c), which is significantly lower than that of the Fe/PbSe junction ($-20.2 \mu\Omega \text{ cm}^2$) (Supplementary Fig. 30). This indicates that Co serves as a more effective diffusion barrier material than Fe in this context. This is the first test and report of the ρ_c value in PbSe, which is also much lower than that of other TE materials, such as $-30 \mu\Omega \text{ cm}^2$ for the Sb/CdSb junction⁶⁸ and $-210 \mu\Omega \text{ cm}^2$ for the Ni/Bi₂Te_{2.7}Se_{0.3} junction⁶⁹. Additionally, we performed detailed interface characterization on the Ag/Co/PbSe leg. No significant diffusion or cracking was observed between the Ag electrode, the Co TEiM, or the PbSe material (Fig. 5a, b), validating the results from our high-throughput screening. Given that the hot side of TE generators operates at high temperatures for extended periods, the heat endurance at the most vulnerable junction of TEiM/TE material is a crucial factor for evaluating device stability. To assess this phenomenon, we conducted aging tests on the Ag/Co/PbSe assembly after annealing at 873 K for 48 h. The results showed that the contact interface retained excellent thermal stability and robust bonding (Supplementary Fig. 31). These characteristics make Co a promising TEiM for manufacturing high-efficiency and reliable TE modules.

To demonstrate the mid-temperature power generation performance of $\text{Pb}_{1-x}\text{Cu}_{2x+y}\text{Se}$, we developed p-type materials with comparable TE performance (Supplementary Fig. 32) and constructed a seven-pair single-stage TE module composed of n-type $\text{Pb}_{0.98}\text{Cu}_{0.043}\text{Se}$ with Co as the TEiM and p-type GeTe with Ni as the TEiM (details in the Supplementary Information). Supplementary Fig. 33 shows the output performance of this single-stage module (10 mm × 10 mm × 4 mm), achieving a maximum η (η_{max}) of -9.6% and a power density of -20 kW m^{-2} at a hot-side temperature (T_{h}) of 740 K. To increase the η_{max} of the TE module, we conducted finite-element simulations to meticulously design and optimize the geometrical configuration of the module, which was segmented with p-type and n-type Bi₂Te₃-based materials (Fig. 5c and Supplementary Fig. 34). We then manufactured the corresponding seven-pair devices (10 mm × 10 mm × 6 mm, inset in Fig. 1d). The current (I)-dependent output voltage (V) and output power (P) of the segmented module at different T_{h} values are shown in Fig. 5d. As T_{h} increases from 450 to 760 K, the open-circuit voltage (V_{oc}) increases from 0.35 to 1.33 V due to the improved $|S|$ of the TE material. P initially increases with current, peaking when the external load resistance matches the module's internal resistance. The measured η_{max} reaches -13.1% at a ΔT of 460 K (Fig. 5e), setting a record for PbSe-based TE modules²⁷.

In conclusion, introducing Cu into Te-free n-type PbSe (*i.e.*, $\text{Pb}_{1-x}\text{Cu}_{2x+y}\text{Se}$) can result in an ultrahigh peak zT of -1.9 . This approach enables electron–phonon decoupling, leading to an extraordinary average power factor exceeding $24 \mu\text{W cm}^{-1}\text{K}^{-2}$ and an ultralow lattice thermal conductivity of $0.25 \text{ W m}^{-1}\text{K}^{-1}$. Notably, we identified an exceptional TE interface material by high-throughput screening. The robust Co/PbSe junction design effectively prevents chemical diffusion and reaction, achieving a low electrical contact resistivity of $-10.9 \mu\Omega \text{ cm}^2$ with excellent durability and stability. Consequently, we manufacture a segmented TE module and achieve a record-high

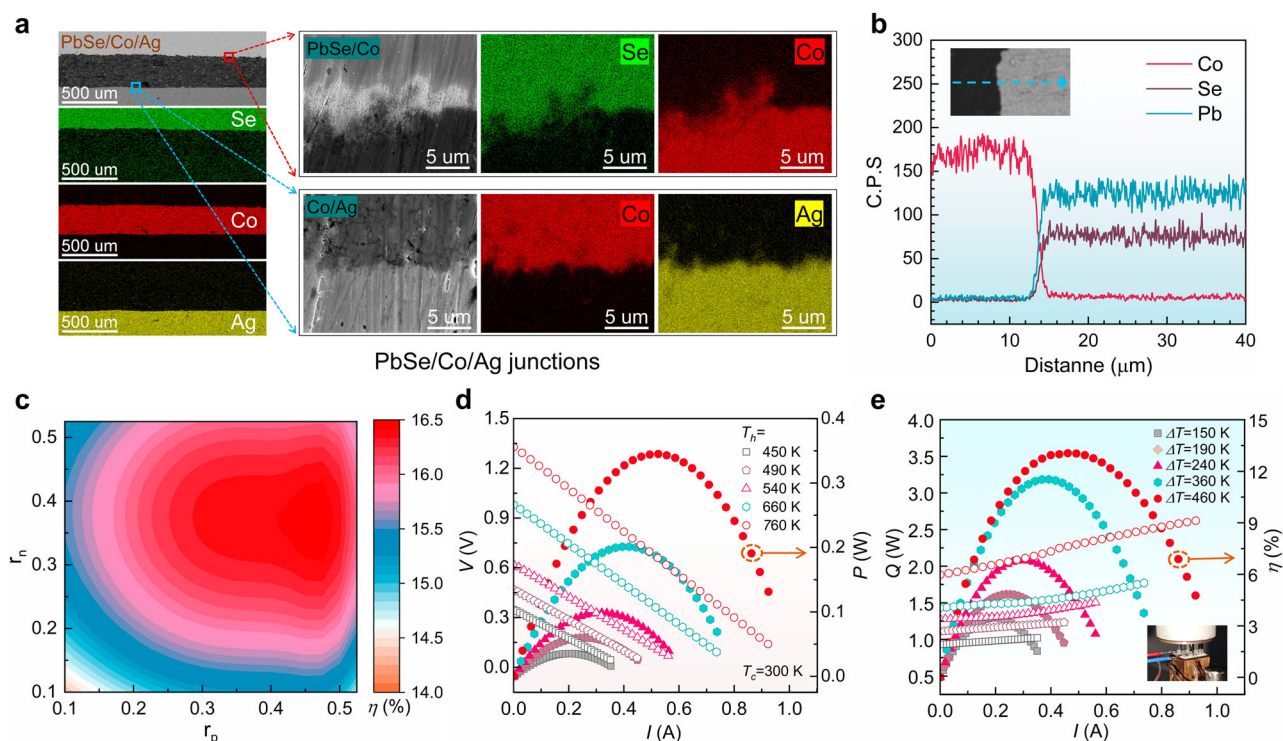


Fig. 5 | The interface microstructures and power generation performance of the segmented module. **a** Scanning electron microscopy (SEM) images and energy dispersive spectroscopy (EDS) mapping of the PbSe/Co/Ag leg. **b** EDS line scan of the Co/PbSe junction. **c** Optimized length ratios of n-type Bi₂Te₃/PbSe (r_n) and

p-type Bi₂Te₃/GeTe (r_p) segments determined by numerical simulation when the hot-side temperature (T_h) and the cool-side temperature (T_c) are 773 and 303 K, respectively. Current-dependent **d** output voltage (V) and output power (P). **e** Heat flow (Q) and conversion efficiency (η) as a function of current.

efficiency of 13.1% at a temperature difference of 460 K. These findings are expected to advance the application of Te-free thermoelectrics.

Methods

Synthesis

High-purity initial materials Pb (99.999%), Se (99.999%), Cu (99.9999%) were weighted according to the stoichiometric composition of PbSe and Pb_{1-x}Cu_{2x+y}Se. Subsequently, the raw materials were sealed in the evacuated quartz tubes ($<10^{-3}$ Pa) and heated up to 1423 K in 6.5 h, held for 8 h, quenched to room temperature, and annealed at 923 K for 100 h. The PbSe and Pb_{1-x}Cu_{2x+y}Se ingots were finely powdered in an agate mortar and then sintered by hot pressing at an axial pressure of 55 MPa and 873 K for 0.5 h to obtain high-density cylindrical samples with a diameter of ~ 12.7 mm (Supplementary Table 5). For the screening of TEIMs, the powder of ten candidate materials (Ti, Zr, V, Cr, Mn, Ni, Nb, Mo, Fe and Co) were co-mixed evenly with pristine PbSe powder in an agate mortar. According to the above Pb_{1-x}Cu_{2x+y}Se sintering parameters, the mixed powders were sintered into a bulk. The weight of each candidate metal powder is about 0.2% of the PbSe.

Characterization

Room-temperature data for XRD were collected utilizing the lab X-ray diffractometer. Synchrotron radiation X-ray characterization was conducted on various advanced beamlines at Beijing Synchrotron Radiation Facility (BSRF) and Shanghai Synchrotron Radiation Facility (SSRF). In-situ variable temperature XRD experiments were performed for Pb_{0.98}Cu_{0.043}Se sample using an incident energy of 40 keV with nitrogen (N₂) as a protective gas in the temperature range from room temperature to 823 K. The 2D XRD patterns were acquired in transmission mode with the PerkinElmer 1621 N flat-panel detector (pixel size $200 \mu\text{m} \times 200 \mu\text{m}$). The XRD data were calibrated with CeO₂ leading to the determination of the sample-to-detector distance. The Cu K-edge and Se K-edge XANES and the EXAFS were conducted in

fluorescence mode or transmission mode using a Si (111) double-crystal monochromator at ambient conditions. The photon energies were calibrated using the first inflection point of the K-edges from metallic Cu foil and elemental selenium, respectively. The topography of TE materials and junctions were investigated using field emission SEM equipped with EDS. Microstructure measurements were performed on the TEM (JEOL-F200) and Cs-corrected STEM (JEOL-NEOARM 200F). The geometrical configuration of the segmented TE module was optimized utilizing the finite element analysis software, where the temperature-dependent σ , S , and κ_{tot} of Bi₂Te₃, PbSe, and GeTe from the experiment were used as an input parameter for the program.

Thermoelectric property measurements

The Hall measurements was conducted utilizing the Van der Pauw method in a high purity He₂. The S and σ of samples were measured simultaneously on a commercial CTA instrument (Cryoall, China). The thermal diffusivity (D) was collected using Netzsch LFA 467. The κ_{tot} was obtained from $\kappa_{\text{tot}} = dDC_p$, where the heat capacity C_p in this work is theoretically evaluated by Debye model, which has been widely used in PbSe systems. The density d is measured by the Archimedes' drainage method. The electronic thermal conductivity κ_{ele} is calculated using the Wiedemann-Franz law: $\kappa_{\text{ele}} = \sigma LT$, where σ represents the experimental electrical conductivity of the samples. The Lorenz number L is determined based on the experimental Seebeck coefficient and the single Kane band (SKB) model. The lattice thermal conductivity κ_{lat} is estimated by subtracting κ_{ele} from the total thermal conductivity κ_{tot} .

Segmented module fabrication

The n-type PbSe legs with Co and Ag on both sides were sintered by one-step hot pressing. The Bi₂Te₃ and GeTe materials were electroplated with Ni as TEIM. The Bi₂Te₃, PbSe and GeTe bulks were cut into

dimensions of about $1.5\text{ mm} \times 1.5\text{ mm} \times 2\text{ mm}$, $1.5\text{ mm} \times 1.5\text{ mm} \times 4\text{ mm}$ and $1.5\text{ mm} \times 1.5\text{ mm} \times 4\text{ mm}$, respectively. After polishing, the high-temperature and low-temperature legs were directly sintered onto copper alumina ceramics using commercial nano-silver paste to assemble 7 pairs of segmented TE module. The copper-wires were welded to the low-temperature side copper electrode.

Data availability

All data necessary to understand and assess this manuscript are shown in the main text and the Supplementary Information. The data that support the findings of this study are available from the corresponding author upon reasonable request. Source data are provided with this paper.

References

1. Pei, Y., Shi, X., LaLonde, A., Wang, H., Chen, L. & Snyder, G. J. Convergence of electronic bands for high performance bulk thermoelectrics. *Nature* **473**, 66–69 (2011).
2. Tan, G., Zhao, L. D. & Kanatzidis, M. G. Rationally designing high-performance bulk thermoelectric materials. *Chem. Rev.* **116**, 12123–12149 (2016).
3. Shi, X. L., Zou, J. & Chen, Z. G. Advanced thermoelectric design: from materials and structures to devices. *Chem. Rev.* **120**, 7399–7515 (2020).
4. Bell, L. E. Cooling, heating, generating power, and recovering waste heat with thermoelectric systems. *Science* **321**, 1457–1461 (2008).
5. Xie, L. et al. Screening strategy for developing thermoelectric interface materials. *Science* **382**, 921–928 (2023).
6. Hu, H. et al. Highly stabilized and efficient thermoelectric copper selenide. *Nat. Mater.* **23**, 527–534 (2024).
7. Wang, H., Pei, Y., LaLonde, A. D. & Snyder, G. J. Weak electron-phonon coupling contributing to high thermoelectric performance in n-type PbSe. *Proc. Natl Acad. Sci. USA* **109**, 9705–9709 (2012).
8. You, L. et al. Boosting the thermoelectric performance of PbSe through dynamic doping and hierarchical phonon scattering. *Energy Environ. Sci.* **11**, 1848–1858 (2018).
9. Qian, X. et al. Synergistically optimizing interdependent thermoelectric parameters of n-type PbSe through alloying CdSe. *Energy Environ. Sci.* **12**, 1969–1978 (2019).
10. Qian, X., Zhou, J. & Chen, G. Phonon-engineered extreme thermal conductivity materials. *Nat. Mater.* **20**, 1188–1202 (2021).
11. Roychowdhury, S. et al. Enhanced atomic ordering leads to high thermoelectric performance in AgSbTe_2 . *Science* **371**, 722–727 (2021).
12. Biswas, K. et al. High-performance bulk thermoelectrics with all-scale hierarchical architectures. *Nature* **489**, 414–418 (2012).
13. Wu, Y. et al. Lattice strain advances thermoelectrics. *Joule* **3**, 1276–1288 (2019).
14. Zhang, J. et al. Extraordinary thermoelectric performance realized in n-type PbTe through multiphase nanostructure engineering. *Adv. Mater.* **29**, 1703148 (2017).
15. Xiao, Y. et al. Remarkable roles of Cu to synergistically optimize phonon and carrier transport in n-type PbTe- Cu_2Te . *J. Am. Chem. Soc.* **139**, 18732–18738 (2017).
16. You, L. et al. Realization of higher thermoelectric performance by dynamic doping of copper in n-type PbTe. *Energy Environ. Sci.* **12**, 3089–3098 (2019).
17. Jia, B. et al. Pseudonanostructure and trapped-hole release induce high thermoelectric performance in PbTe. *Science* **384**, 81–86 (2024).
18. Chen, Z. et al. Lattice dislocations enhancing thermoelectric PbTe in addition to band convergence. *Adv. Mater.* **29**, 1606768 (2017).
19. Amatya, R. & Ram, R. J. Trend for thermoelectric materials and their earth abundance. *J. Electron Mater.* **41**, 1011–1019 (2012).
20. Zhou, C. & Chung, I. Nanoscale defect structures advancing high performance n-type PbSe thermoelectrics. *Coord. Chem. Rev.* **421**, 213437 (2020).
21. Zhu, Y. et al. Multiple valence bands convergence and strong phonon scattering lead to high thermoelectric performance in p-type PbSe. *Nat. Commun.* **13**, 4179 (2022).
22. Tan, G. et al. All-Scale hierarchically structured p-type PbSe alloys with high thermoelectric performance enabled by improved band degeneracy. *J. Am. Chem. Soc.* **141**, 4480–4486 (2019).
23. Jiang, B. et al. Entropy engineering promotes thermoelectric performance in p-type chalcogenides. *Nat. Commun.* **12**, 3234 (2021).
24. Xu, L. et al. Dense dislocations enable high-performance PbSe thermoelectric at low-medium temperatures. *Nat. Commun.* **13**, 6449 (2022).
25. Ge, B. et al. Engineering an atomic-level crystal lattice and electronic band structure for an extraordinarily high average thermoelectric figure of merit in n-type PbSe. *Energy Environ. Sci.* **16**, 3994–4008 (2023).
26. Zhou, C. et al. Defect engineering for high-performance n-type PbSe thermoelectrics. *J. Am. Chem. Soc.* **140**, 9282–9290 (2018).
27. Jiang, B. B. et al. High-entropy-stabilized chalcogenides with high thermoelectric performance. *Science* **371**, 830–834 (2021).
28. Xing, T. et al. High efficiency GeTe-based materials and modules for thermoelectric power generation. *Energy Environ. Sci.* **14**, 995–1003 (2021).
29. Luo, Z. et al. Soft phonon modes from off-center Ge atoms lead to ultralow thermal conductivity and superior thermoelectric performance in n-type PbSe-GeSe. *Energy Environ. Sci.* **11**, 3220–3230 (2018).
30. Chen, Z. et al. Vacancy-induced dislocations within grains for high-performance PbSe thermoelectrics. *Nat. Commun.* **8**, 13828 (2017).
31. Zhang, Q. et al. Enhancement of thermoelectric figure-of-merit by resonant states of aluminum doping in lead selenide. *Energy Environ. Sci.* **5**, 5246–5251 (2012).
32. Qin, Y. et al. Grid-planification enables medium-temperature PbSe thermoelectrics to cool better than Bi_2Te_3 . *Science* **383**, 1204–1209 (2024).
33. Wang, S. et al. Realizing high-performance thermoelectric modules through enhancing the power factor by optimizing the carrier mobility in n-type PbSe crystals. *Energy Environ. Sci.* **17**, 2588–2597 (2024).
34. Pang, H. et al. Realizing ultrahigh thermoelectric performance in n-type PbSe through lattice planification and introducing liquid-like Cu ions. *Adv. Funct. Mater.* **34**, 2401716 (2024).
35. Deng, Q. et al. Unique semi-coherent nanostructure advancing thermoelectrics of n-type PbSe. *Adv. Funct. Mater.* **34**, 2310073 (2023).
36. Wang, S. et al. High carrier mobility and promising thermoelectric module performance of n-type PbSe crystals. *Small* **20**, 2400866 (2024).
37. Blöchl, P. E. Projector augmented-wave method. *Phys. Rev. B* **50**, 17953–17979 (1994).
38. Kresse, G. & Furthmüller, J. Efficient iterative schemes for ab initio total-energy calculations using a plane-wave basis set. *Phys. Rev. B* **54**, 11169–11186 (1996).
39. Perdew, J. P., Burke, K. & Ernzerhof, M. Generalized gradient approximation made simple. *Phys. Rev. Lett.* **77**, 3865–3868 (1996).
40. Bu, Z. et al. Dilute Cu_2Te -alloying enables extraordinary performance of r-GeTe thermoelectrics. *Mater. Today, Phys.* **9**, 100096 (2019).
41. Voneshen, D. J., Walker, H. C., Refson, K. & Goff, J. P. Hopping time scales and the phonon-liquid electron-crystal picture in thermoelectric copper selenide. *Phys. Rev. Lett.* **118**, 145901 (2017).
42. Sarma, B. B., Maurer, F., Doronkin, D. E. & Grunwaldt, J.-D. Design of single-atom catalysts and tracking their fate using operando and advanced X-ray spectroscopic tools. *Chem. Rev.* **123**, 379–444 (2023).

43. Qiu, W. et al. Structure family and polymorphous phase transition in the compounds with soft sublattice: Cu_2Se as an example. *J. Chem. Phys.* **144**, 194502 (2016).
44. Qian, X. et al. Contrasting roles of small metallic elements M (M = Cu, Zn, Ni) in enhancing the thermoelectric performance of n-type $\text{PbM}_{0.01}\text{Se}$. *J. Mater. Chem. A* **8**, 5699–5708 (2020).
45. Sun, J. et al. Defect chemistry engineering promotes the dopability of Cu for an extraordinary thermoelectric performance of hole-doped PbSe with resonant states. *Chem. Mater.* **35**, 4366–4374 (2023).
46. Yu, Y. et al. Ostwald ripening of Ag_2Te precipitates in thermoelectric PbTe: effects of crystallography, dislocations, and interatomic bonding. *Adv. Energy Mater.* **14**, 2304442 (2024).
47. Ratke L., Voorhees P. W. *Growth and Coarsening: Ostwald Ripening in Material Processing*. Springer Science & Business Media (2002).
48. Liu, H. et al. Copper ion liquid-like thermoelectrics. *Nat. Mater.* **11**, 422–425 (2012).
49. Liu, H. et al. Ultrahigh thermoelectric performance by electron and phonon critical scattering in $\text{Cu}_2\text{Se}_{1-x}\text{S}_x$. *Adv. Mater.* **25**, 6607–6612 (2013).
50. Zhou, Z. et al. Compositing effects for high thermoelectric performance of Cu_2Se -based materials. *Nat. Commun.* **14**, 2410 (2023).
51. Yuan, H.-L., Wang, K., Hu, H., Yang, L., Chen, J. & Zheng, K. Atomic-scale observation of grain boundary dominated unsynchronized phase transition in polycrystalline Cu_2Se . *Adv. Mater.* **34**, 2205715 (2022).
52. Min, J., Sagotra, A. K. & Cazorla, C. Large barocaloric effects in thermoelectric superionic materials. *Phys. Rev. Mater.* **4**, 015403 (2020).
53. Ge, B. et al. Atomic level defect structure engineering for unusually high average thermoelectric figure of merit in n-type PbSe rivalling PbTe. *Adv. Sci.* **19**, 2203782 (2022).
54. Zhou, C. et al. Exceptionally high average power factor and thermoelectric figure of merit in n-type PbSe by the dual incorporation of Cu and Te. *J. Am. Chem. Soc.* **142**, 15172–15186 (2020).
55. Kane, E. O. Band structure of indium antimonide. *J. Phys. Chem. Solids* **1**, 249–261 (1957).
56. Heremans, J. P. et al. Enhancement of thermoelectric efficiency in PbTe by distortion of the electronic density of states. *Science* **321**, 554–557 (2008).
57. Gayner, C. & Amouyal, Y. Energy filtering of charge carriers: current trends, challenges, and prospects for thermoelectric materials. *Adv. Funct. Mater.* **30**, 201901789 (2020).
58. Zhao, W. et al. Superparamagnetic enhancement of thermoelectric performance. *Nature* **549**, 247–251 (2017).
59. Seto, J. Y. W. The electrical properties of polycrystalline silicon films. *J. Appl. Phys.* **46**, 5247–5254 (1975).
60. Tian, Z. et al. Phonon conduction in PbSe, PbTe, and $\text{PbTe}_{1-x}\text{Se}_x$ from first-principles calculations. *Phys. Rev. B* **85**, 184303 (2012).
61. Zhang, Q. et al. Enhancement of thermoelectric performance of n-type PbSe by Cr doping with optimized carrier concentration. *Adv. Energy Mater.* **5**, 1401977 (2015).
62. Zhang, Q. et al. Study of the thermoelectric properties of lead selenide doped with boron, gallium, indium, or thallium. *J. Am. Chem. Soc.* **134**, 17731–17738 (2012).
63. Zhou, C. et al. High-performance n-type $\text{PbSe-Cu}_2\text{Se}$ thermoelectrics through conduction band engineering and phonon softening. *J. Am. Chem. Soc.* **140**, 15535–15545 (2018).
64. Luo, Z.-Z. et al. Strong valence band convergence to enhance thermoelectric performance in PbSe with two chemically independent controls. *Angew. Chem. Int. Ed.* **60**, 268–273 (2021).
65. Androulakis, J., Todorov, I., He, J., Chung, D. Y., Dravid, V. & Kanatzidis, M. Thermoelectrics from abundant chemical elements: high-performance nanostructured PbSe-PbS. *J. Am. Chem. Soc.* **133**, 10920–10927 (2011).
66. Agne, M. T., Hanus, R. & Snyder, G. J. Minimum thermal conductivity in the context of diffuson-mediated thermal transport. *Energy Environ. Sci.* **11**, 609–616 (2018).
67. Gu, M. et al. A high-throughput strategy to screen interfacial diffusion barrier materials for thermoelectric modules. *J. Mater. Res.* **34**, 1179–1187 (2019).
68. Bu, Z. et al. A record thermoelectric efficiency in tellurium-free modules for low-grade waste heat recovery. *Nat. Commun.* **13**, 237 (2022).
69. Liu, W. S. et al. Understanding of the contact of nanostructured thermoelectric n-type $\text{Bi}_2\text{Te}_{2.7}\text{Se}_{0.3}$ legs for power generation applications. *J. Mater. Chem. A* **1**, 13093–13100 (2013).

Acknowledgements

We acknowledge support from the National Key Research and Development Program of China (Grant No. 2022YFB3803900), the Regional Innovation Cooperation Project of the Sichuan Science and Technology Program (Grant No. 2024YFHZ0204), and the Innovation Research Program of Sichuan University (Grant No. 2020SCUNL112). Z.-G.C. thanks the Australian Research Council, the HBIS-UQ Innovation Centre for Sustainable Steel project, and the QUT Capacity Building Professor Program. M.L. and Z.-G.C. thank the National Computational Infrastructure for providing the computational allocation (Project wk98). C.W. and Y.C. are grateful for the research computing facilities offered by ITS and HKU. The authors thank the 4B9A beamline station at Beijing Synchrotron Radiation Facility (BSRF), the BL17B station of National Facility for Protein Science in Shanghai (NFPS) and BLO2U2, BL11B, BL13HB, BL14W1 and BL16U1 stations at Shanghai Synchrotron Radiation Facility (SSRF) and the User Experiment Assist System of SSRF for the help in characterizations.

Author contributions

Z.-G.C. and R.A. conceived and designed this work. Q.D. prepared the PbSe materials, measured the thermoelectric properties and designed device structures; fabricated the modular devices; and measured the performance. X.B.T. prepared the GeTe materials and measured the thermoelectric properties. R.H.L. performed the device numerical simulation. C.W., Y.C., and M.L. performed the first-principles calculations. H.-L.D. conducted the synchrotron radiation experiments. Q.D., X.-L.S., H.-L.D., R.A., and Z.-G.C. discussed the results and wrote the manuscript.

Competing interests

The authors declare no competing interests.

Additional information

Supplementary information The online version contains supplementary material available at <https://doi.org/10.1038/s41467-025-56003-9>.

Correspondence and requests for materials should be addressed to Hongliang Dong, Ran Ang or Zhi-Gang Chen.

Peer review information *Nature Communications* thanks F. Caballero-Briones who co-reviewed with Fernanda Gonzalez-Moreno and the other anonymous reviewer(s) for their contribution to the peer review of this work. A peer review file is available.

Reprints and permissions information is available at <http://www.nature.com/reprints>

Publisher's note Springer Nature remains neutral with regard to jurisdictional claims in published maps and institutional affiliations.

Open Access This article is licensed under a Creative Commons Attribution-NonCommercial-NoDerivatives 4.0 International License, which permits any non-commercial use, sharing, distribution and reproduction in any medium or format, as long as you give appropriate credit to the original author(s) and the source, provide a link to the Creative Commons licence, and indicate if you modified the licensed material. You do not have permission under this licence to share adapted material derived from this article or parts of it. The images or other third party material in this article are included in the article's Creative Commons licence, unless indicated otherwise in a credit line to the material. If material is not included in the article's Creative Commons licence and your intended use is not permitted by statutory regulation or exceeds the permitted use, you will need to obtain permission directly from the copyright holder. To view a copy of this licence, visit <http://creativecommons.org/licenses/by-nc-nd/4.0/>.

© The Author(s) 2025